Optical Coherence Tomography for the Inspection of Plasma-Sprayed Ceramic Coatings

J. Veilleux, C. Moreau, D. Lévesque, M. Dufour, and M. Boulos

Optical coherence tomography (OCT) is evaluated as a potential technique for microstructure characterization of plasma-sprayed ceramic coatings. OCT combines the principles of low-coherence interferometry and optical heterodyne detection to obtain both a high axial resolution and a high sensitivity to weakly backscattered light. It can be used to accurately locate interfaces where the refractive index changes abruptly within translucent materials. Therefore, OCT should be sensitive to interlamellar pores and splat interfaces within plasma-sprayed ceramic coatings. In the present work, OCT cross-sectional images of thin yttria-stabilized zirconia (YSZ) coatings are considered. The interferogram envelopes forming the collected images are analyzed individually to successfully gather information related to light attenuation inside the coatings. This light attenuation is shown to be related to the density of interfaces within the coatings as well as to the material oxidation state. The envelope analysis also allows the evaluation of the refractive index of the YSZ nontransformable tetragonal phase.

1. Introduction

It is now well established that plasma-sprayed ceramic coatings are appreciably contributing to the reduction of premature material degradation in harsh environment (Ref 1). For example, they act as thermal barrier and protective coatings against wear and corrosion in the aeronautical (Ref 2) and automotive (Ref 3) industries. As well, they are used as biocompatible coatings deposited on biomedical implants (Ref 4) and as solid oxide fuel cell components (electrodes and electrolyte) (Ref 5). In many of these applications currently in development, the quality of plasma-sprayed ceramic coatings is critical to ensure proper and safe use of the coated parts to avoid catastrophic failure. In other words, they are becoming prime reliant. However, plasma spraying is a stochastic process

J. Veilleux and **M. Boulos,** Department of Chemical Engineering, University of Sherbrooke, 2500, de l'Université Blvd., Sherbrooke, QC, Canada, J1K 2R1; **C. Moreau, D. Lévesque** and **M. Dufour,** Industrial Materials Institute, National Research Council Canada, 75, de Mortagne, Boucherville, QC, Canada, J4B 6Y4. Contact e-mail: christian.moreau@imi.cnrc-nrc.gc.ca.

through which the feedstock ceramic particles are melted and accelerated. Melted droplets then impinge the substrate where they form rapidly solidified splats. The resulting microstructure of this random coating build-up is characterized by the existence of interlamellar pores, globular pores, splat interfaces, and intrasplat cracks which are all known to significantly influence coatings thermal conductivity and mechanical properties (Ref 6). Therefore, a close control of the coating microstructure is sought to meet the requirements of the target application. It would be of high practical interest to develop a nondestructive evaluation (NDE) technique to observe and characterize the microstructure (and especially the porosity) of plasma-sprayed ceramic coatings.

In fact, existing NDE techniques for characterization of plasma-sprayed ceramic coatings are not well suited for direct porosity measurements. Ultrasonic techniques (Ref 7) and acoustic microscopy (Ref 8) show sensitivity to coating porosity via the attenuation of the echo coming from the substrate (Ref 9), but they share two major shortcomings: they require immersion of the coated part in a liquid to ensure proper coupling of sound waves and they have a limited resolution (on the order of 10^{-3} m). Laser ultrasonics makes it possible to avoid the problem of immersion coupling and lends itself better to an in situ use. According to this technique, a short and powerful laser pulse is directed on the surface of the sample to generate ultrasounds (Ref 10). Then, a second laser pulse of longer duration is used to follow the displacements of the coating surface. These displacements are associated to the echoes of waves that were propagated inside the coating. As mentioned earlier, the microstructural information obtained from ultrasonic inspection techniques remains relatively limited, except for the observation of

delamination at the coating/substrate interface (Ref 11) and for the determination of the coating elastic modulus. The latter strongly depends on the quality of splat interfaces (Ref 12) and on interlamellar porosity. However, this sensitivity is insufficient to overcome the implementation difficulties of a traditional immersion system or of laser ultrasonics.

Thermal wave techniques are also interesting to probe the quality of the coating splat interfaces. Indeed, heat propagation inside a coating is strongly influenced by the quality of these interfaces (Ref 13, 14). In infrared thermography (Ref 15), a portion of the coating is heated by a laser beam and sensors (pyrometers) measure the local temperature changes on the coating surface. The presence of defects alters heat diffusion, which results in small temperature variations at the surface of the coating. Consequently, this technique could hardly be implemented inside projection rooms where temperature measurements would be disturbed by the surrounding infrared radiation (Ref 10). Moreover, the surface of the coating must have a constant emissivity (absence of oil traces, of dirtiness, of oxidation, or reduction), since the sensors would otherwise detect these differences in emissivity rather than the presence of defects (Ref 16).

Small-angle neutron scattering (SANS) constitutes another NDE technique recently applied to ceramic coatings. The principle of the method lies in neutron scattering at ceramic/pore interfaces, where a change in neutron scattering length occurs. Scattered neutrons are then collected to determine the total porosity surface per unit volume in the sample and the anisotropy of the diffusion pattern makes it possible to distinguish various types of porosity (e.g., splat interfaces, interlamellar pores, and globular pores) (Ref 17-19). Two geometries can be used to collect the neutrons: in transmission (applicable to self-standing coatings with a thickness up to 3 mm) and in reflection (applicable to on-substrate ceramic coatings less than 250 µm thick). For the latter geometry, the effective neutron penetration depth reaches only 40 µm. Porosity measurements obtained with this technique corroborates the results obtained by SEM image analysis of ceramic coatings (Ref 20). However, SANS requires sophisticated nuclear installations to produce and confine the neutrons in a beam whose handling requires important protection measures, which limits its application to industrial environments. In addition, none of the characterization techniques quoted previously offers the possibility to characterize the microstructure of ceramic coatings in situ.

In this regard, optical coherence tomography (OCT), a technology that was predominantly developed for cross-sectional imaging of biological system microstructure (Ref 21), has some promising features. In fact, OCT presents an axial resolution of the same order of magnitude as the splat thickness as well as a good sensitivity to ceramic/air interfaces. In particular, OCT is expected to be sensitive to interlamellar contact and to globular porosity. Although briefly discussed by Moreau (Ref 10), the use of OCT to characterize plasma-sprayed thermal barrier coatings has not been extensively explored. However, some interesting studies illustrate OCT inspection performances by describing its capability to image polymer matrix composites (Ref 22), to detect subsurface defects in Si_3N_4 ceramic balls (Ref 23), and to measure the thickness up to 50 µm of EB-PVD thermal barrier coatings (Ref 24, 25).

In the present work, OCT interferogram envelopes of four different yttria-stabilized zirconia (YSZ) coatings are collected and analyzed to evaluate light attenuation inside coatings. The influence of the density of interfaces within coatings (overall porosity percentage and splat thickness) and of the material oxidation state on light attenuation is studied. In another set of experiments, OCT is used to evaluate the refractive index of YSZ nontransformable tetragonal phase.

1.1 Principles of OCT

As shown in Fig. 1, an OCT system is actually based on a Michelson interferometer. The light emitted by a broadband source (superluminescent diode—SLD) is divided at a beam splitter (BS) into two distinct optical paths that are, respectively, oriented towards the reference mirror and the sample. When the light returns, both the sample backscattered field and the reference field will combine to produce an interference signal (or interferogram) only if the optical path length mismatch between reference and sample arms is shorter than the light coherence length. This interferogram is collected by the photodetector, amplified and digitally processed (filtered and demodulated). By recording the interference signal amplitude and phase as the reference mirror is synchronously translated, the axial profile of the sample backscattering properties can be obtained. The axial resolution in this profile depends on the coherence length of the light source. Consequently, a high resolution can be achieved independently of the beam focusing conditions, thus of the sample arm optics. In fact, for a light source with a Gaussian spectral distribution, it can be shown (Ref 26) that the axial resolution $\Delta\xi$ of the OCT system is inversely proportional to the bandwidth $\Delta\lambda$ of the power spectrum centered at a wavelength λ:
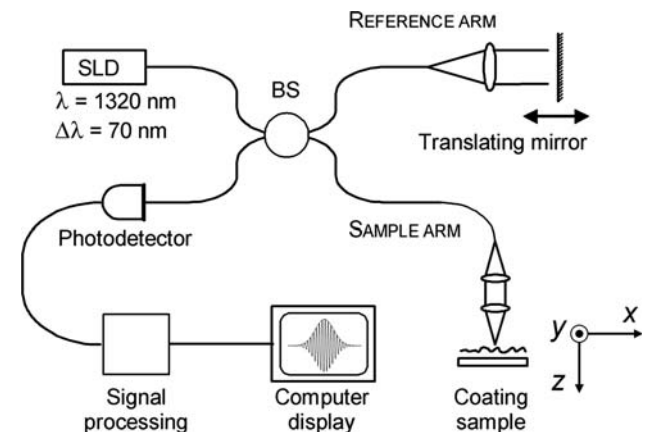

Fig. 1 Schematic representation of the OCT system based on a Michelson interferometer used in the present work

$$\Delta\xi = \left(\frac{2\ln 2}{\pi}\right)\left(\frac{\lambda^2}{\Delta\lambda}\right). \tag{Eq 1}$$

2. Experimental Procedure

2.1 Plasma Spraying

Four different YSZ coatings were sprayed on a grit-blasted steel substrate using a Sulzer Metco F4-MB plasma torch (Sulzer Metco Inc., Westbury, NY), which uses external radial powder injection and swirl flow gas injection. Argon (primary gas flow rate of 35 L/min) and hydrogen (secondary gas flow rate of 12 L/min) were used as the plasma gas mixture. The power input was held to 28 or 35 kW (referred to as *L* for low and *H* for high, respectively), with power variation being obtained through current increase from 425 to 550 A. Two commercial Amperit (H.C. Starck Inc., Newton, MA) YSZ feedstock powders were selected: Amperit 825.0 (7 wt.% YSZ, $-22+5$ μm) and Amperit 825.1 (7 wt.% YSZ, $-45+22$ μm), referred to as *F* for fine and *C* for coarse particles, respectively. They were injected at a constant feed rate of 25 g/min with argon as carrier gas (3 L/min), using a conventional powder feeder (Roto-feed powder hopper model 1252, Praxair Surface Technologies, Indianapolis, IN). In each case, the plasma torch stand-off distance was kept constant at 120 mm. Finally, during spraying, the samples were continuously cooled down with an air jet to maintain the surface temperature between 175 °C and 225 °C. Spraying conditions for the four YSZ coatings deposited are summarized in Table 1. In-flight mean particle temperature and mean particle velocity were measured using a DPV-2000 sensor (Tecnar Automation Ltd., St-Bruno, Quebec, Canada) and are given in Table 2.

Coating thickness and porosity were both determined by image analysis of the SEM micrographs (JEOL JSM-6100, JEOL, Peabody, MA) shown in Fig. 2 for a magnification of 500×. The same standard protocol, optimized for ceramic thermal barrier coatings, was used for the metallographic preparation of all samples. The values given in Table 3 correspond to an average of ten measurements for which the corresponding statistical errors are also given. A field-emission gun SEM (Hitachi S-4700, Hitachi, Rexdale, Ontario, Canada) was used to characterize coating splat microstructure. An example is shown in Fig. 3 for a fracture of samples C-H and F-H.

As expected, the coatings built under higher plasma torch power present a lower porosity level. Moreover, the larger powder produces thicker splats as it can be seen in Fig. 3. Indeed, splats of 5 μm are observed in Fig. 3(a) whereas splats in Fig. 3(b) have a maximum thickness of 3 μm. These differences are expected to significantly affect the interferogram envelopes collected by OCT. In particular, different interlamellar pores and splat interfaces should influence light attenuation.

2.2 Optical Coherence Tomography

The coatings were imaged with the OCT system shown in Fig. 1. Unless otherwise stated, YSZ coatings were observed as sprayed, without any special preparation. The optical source coupled into the interferometer was a superluminescent diode (Covega SLD-236, Covega, Jessup, MD) emitting over a 70 nm wide bandwidth centered at a wavelength of 1320 nm. Thus, the system axial resolution calculated from Eq. 1 is 11 μm. The maximum emitted power was 17 mW from which only 10% was actually coupled into the interferometer to avoid saturation of the photodetector. In the sample arm, a 2 mm wide collimated beam was focused onto the sample coating surface using a lens with a focal length of 25 mm. The resulting transverse resolution of the system is 22 μm. The backscattered signal amplitude is recorded as a function of the optical path, with a step size of 1 μm, to form an interferogram envelope (analogous to an A-scan in ultrasonic imaging). For each coating sample, 1200 envelopes were collected to form a single cross-sectional image (B-scan) by scanning along the *x*-axis, and the procedure was repeated ten times. The step size between two successive interferogram envelopes was 1 μm, and the separation between two cross-sectional images was 10 μm. The latter step of 10 μm was chosen to reduce the overlapping (oversampling) between two successive cross-sectional images, but could be reduced to 1 μm in a context of 3-D imaging. Overall, ten cross-sectional images with dimensions of 1.2 mm wide and 1.8 mm deep were collected for each sample.

Table 1 Plasma-spraying conditions

Condition	Value			
Gun	F4-MB			
Primary gas flow rate Argon, L/min	35			
Secondary gas flow rate Hydrogen, L/min	12			
Carrier gas flow rate Argon, L/min	3			
Powder feed rate, g/min	25			
Injection	Radial, external from top			
Stand-off distance, mm	120			
Substrate temperature, °C	Between 175 and 225			
Sample ID	C-H	C-L	F-H	F-L
YSZ powder, Amperit	825.1	825.1	825.0	825.0
Current, A	550	425	550	425
Power, kW	35	28	35	28

Table 2 Mean (μ) and standard deviation (σ) of in-flight particle temperature and velocity distributions

Condition	C-H	C-L	F-H	F-L
μ-Temperature, °C	2758	2678	2712	2659
σ-Temperature, °C	183	172	183	171
μ-Velocity, m/s	200	180	234	217
σ-Velocity, m/s	32	37	39	37

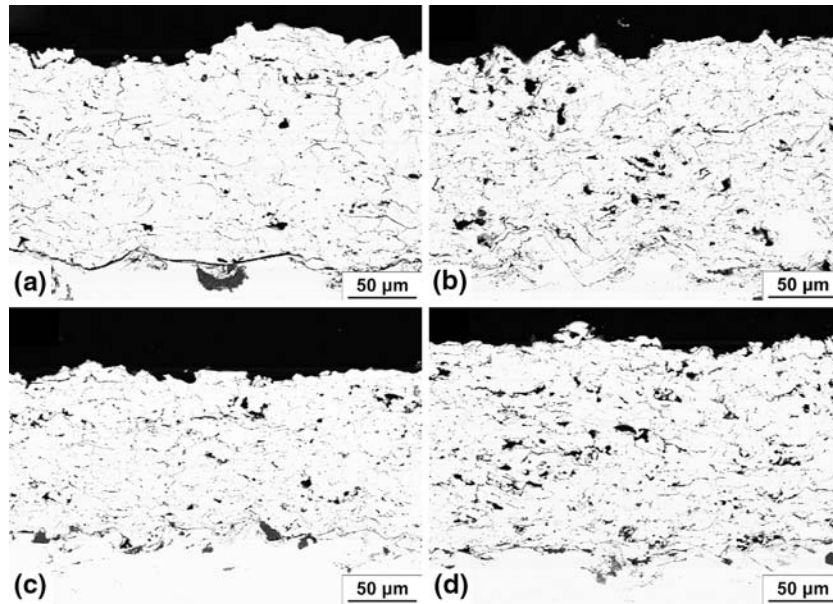Diagnostics were performed at a 120 mm stand-off distance

Fig. 2 SEM micrographs showing the different levels of porosity for the coating samples (a) C-H—Coarse powder (Amperit 825.1) and High plasma torch power (35 kW), (b) C-L—Coarse powder (Amperit 825.1) and Low plasma torch power (28 kW), (c) F-H—Fine powder (Amperit 825.0) and High plasma torch power (35 kW) and (d) F-L—Fine powder (Amperit 825.0) and Low plasma torch power (28 kW)
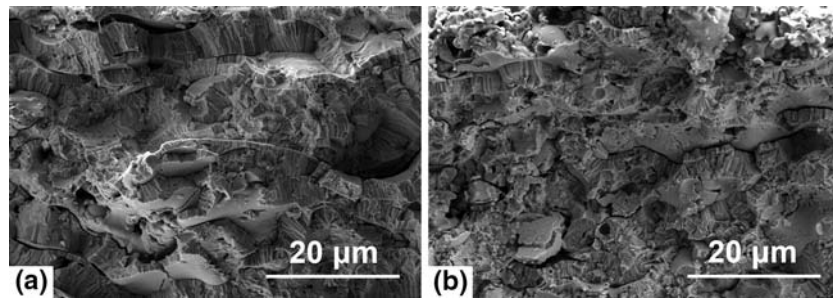

Fig. 3 SEM fractographies showing splat microstructure of samples (a) C-H—Coarse powder (Amperit 825.1) and High plasma torch power (35 kW) and (b) F-H—Fine powder (Amperit 825.0) and High plasma torch power (35 kW)

Table 3 Coating thickness and porosity

Condition	C-H	C-L	F-H	F-L
Coating thickness, μm	115±6	157±9	100±7	152±7
Porosity, %	4.6±0.2	7.8±0.2	5.3±0.2	8.6±0.3

The above values were obtained from $n = 10$ micrographs. The errors given are the statistical errors ($\sigma/n^{1/2}$)

3. Results and Discussion

3.1 Light Attenuation

OCT cross-sectional imaging of YSZ coatings was performed and images of two coatings (with the (a) largest and (b) smallest light-penetration depth, respectively) are shown in Fig. 4. The grayscale is divided into 256 levels to plot the matrix B of the normalized logarithmic amplitude given by

$$B = \frac{\log_{10}(A)}{\max\left[\log_{10}(A)\right]}, \qquad (\text{Eq 2})$$

where A stands for the cross-sectional image amplitude as collected by the OCT system and max[] gives the maximum value of the expression inside the brackets. When plotting B (linear mapping of amplitude values over the 256 level grayscale), 1% of lower and higher amplitudes are saturated to 0 and 1, respectively.

Even if the coatings are relatively thin, the coating/ substrate interface cannot be identified in the OCT images. Peaks coming from this interface are most probably lost among multiple scattering events and speckle. Speckle is a form of coherent noise that appears in OCT when two or more scattering sites in the sample volume send back waves that reach some point on the detector out of phase within a time interval less than the coherence time of the source (Ref 27). Besides these observations, the global
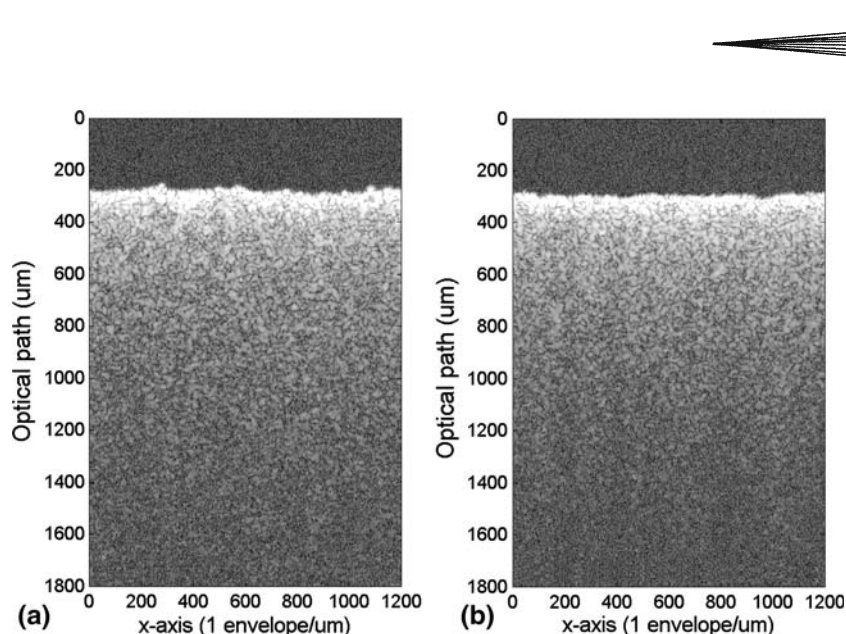
Fig. 4 OCT cross-sectional images of two samples showing normalized logarithmic amplitude as a function of optical path for 1200 interferogram envelopes separated by a step size of 1 μm. (a) C-L—Coarse powder (Amperit 825.1) and Low plasma torch power (28 kW), (b) F-H—Fine powder (Amperit 825.0) and High plasma torch power (35 kW)

light attenuation (which can be observed by the transition from light gray to dark gray) seems quite similar for the coatings. However, statistically significant differences exist between the samples, as discussed below.

The light attenuation inside coatings results from a combination of scattering and absorption events that occur along the optical path of the sample beam, and therefore depends on coating microstructure. Since the YSZ absorption at $\lambda = 1.32$ μm is relatively small (when compared to scattering) and because forward scattering is important, the general Beer-Lambert law of attenuation could not be directly applied to retrieve an attenuation coefficient or a characteristic light penetration depth. Indeed, the observed light attenuation inside coatings differs greatly from an exponential decay (results not shown). Similar results were reported by Yadlowsky et al. (Ref 28) when modeling OCT in heterogeneous tissue. Moreover, it requires a time-consuming algorithm to identify, onto the logarithmic amplitude versus optical path plot, the interferogram peaks that are needed to fit a straight line from which the attenuation coefficient can be evaluated. For these reasons, a different approach was chosen to estimate the light attenuation.

As a simple statistical measure of light penetration inside coatings, the centroid of the envelope amplitude is calculated by analogy to a mass center. The centroid optical position, C, is given by

$$C = \frac{\sum\limits_{i=0}^{N} z_i A_i}{\sum\limits_{i=0}^{N} A_i}, \qquad (\text{Eq 3})$$

where z_i is the optical position of the ith point on an interferogram envelope (with $z_i = \Delta i$, Δ being the acquisition step size of 1 μm), A_i is the signal amplitude collected

at this position and N is the number of points per interferogram envelope. It can be easily shown that, for an exponentially decaying signal, the centroid optical position corresponds exactly to the physical definition of the characteristic light penetration depth δ for a sufficiently large N, that is, for a window length $N\Delta > 7.5\delta$. Therefore, it should be mentioned that the window length would affect the centroid position, just as the position of a mass center would be affected by the length of the considered object.

The centroid calculation is directly applicable to each interferogram envelope. Thus, the implemented algorithm directly uses Eq 3 to calculate the centroid position C_j for each envelope j forming a cross-sectional image, with $N = 1800$ points and $N\Delta = 1800$ μm. The procedure is repeated for all interferogram envelopes (e.g., 1200) and an average value is calculated. This centroid calculation proves to be more robust than the slope tracing onto the logarithmic amplitude signal. In fact, fluctuations in individual centroid position for the 1200 envelopes taken along a cross-sectional image are relatively small (results not shown). Furthermore, variations in the average centroid position between the ten cross-sectional images taken from one sample are smaller than 4%, as shown in Fig. 5(a). Moreover, this pragmatic evaluation of light penetration stays valid when the effects of multiple scattering appear, even though its precise physical interpretation is more difficult to establish in that case.

Figure 5(b) shows significant differences between the average centroid positions taken over ten cross-sectional images for the four YSZ coatings. The following two observations can be drawn. First, without considering the porosity level, the average centroid position is larger for the coarse (C) coatings. Second, the average centroid position is larger in coatings produced at lower plasma torch power (L). Both factors can be justified by the

number of air/ceramic interfaces crossed by the sample beam along its optical path. Indeed, since each crossed interface scatters light, the smaller their number the larger the penetration is. The latter remark is especially true when noting the very small collection angle (0.005 steradian) of backscattered light in the OCT system used. Randomly scattered light at larger angle is not collected.

Therefore, knowing that the number of interfaces per unit length is larger for the fine coatings (they contain thinner splats due to smaller droplets with higher mean velocity), one can explain the observed stronger attenuation. On the other hand, coatings produced at lower plasma torch power are more porous (as determined by SEM image analysis) and have fewer interfaces from which light can be scattered. In fact, when the light beam penetrates a globular or an interlamellar pore, no scattering occurs until it reaches the splat located at the bottom of the pore. In addition, fewer interfaces are found in F-L and C-L coatings since their average splat thickness is larger (owing to lower mean particle temperature and velocity when the torch power is decreased).

3.2 YSZ Absorption in the Near IR

In the previous analysis, the YSZ light absorption was neglected in a first approximation when considering OCT signal attenuation. However, this factor can also contribute to light attenuation inside YSZ coatings. As shown by Debout et al. (Ref 29), the oxygen losses that occur in YSZ during the deposition process (which result in darker coatings (Ref 30)) increase significantly light absorption in the near IR range. Therefore, it is relevant to anneal the coatings and to collect new OCT cross-sectional images to evaluate the real contribution of absorption on OCT signal attenuation. Annealing of the coatings was performed at 600 °C for 8 h to compensate the oxygen losses. Both the as-sprayed and annealed coatings were then imaged using the OCT system described earlier, but the scanning parameters were slightly changed as compared to the previous ones, having a region of 2 mm wide and 2.4 mm deep being probed for each cross-sectional image. Light attenuations inside the as-sprayed and annealed coatings were then compared by calculating the average centroid optical position of the cross-sectional images. The results are shown in Fig. 6.
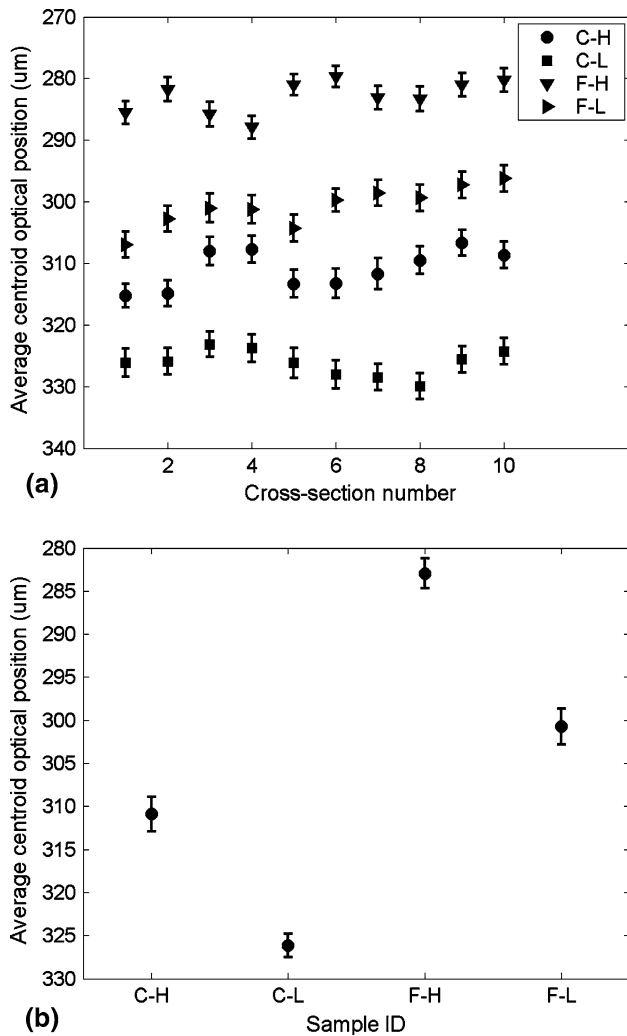

Fig. 5 (a) Variations of the average centroid position for ten cross-sectional images of the four YSZ coatings. (b) Comparison of the average centroid position (calculated from Fig. 5a) for the coating samples. For both (a) and (b), the error bars shown are the statistical error made on the mean value calculated ($\sigma/n^{1/2}$). Again, we have C-H—Coarse powder (Amperit 825.1) and High plasma torch power (35 kW), C-L—Coarse powder (Amperit 825.1) and Low plasma torch power (28 kW), F-H—Fine powder (Amperit 825.0) and High plasma torch power (35 kW) and F-L—Fine powder (Amperit 825.0) and Low plasma torch power (28 kW)
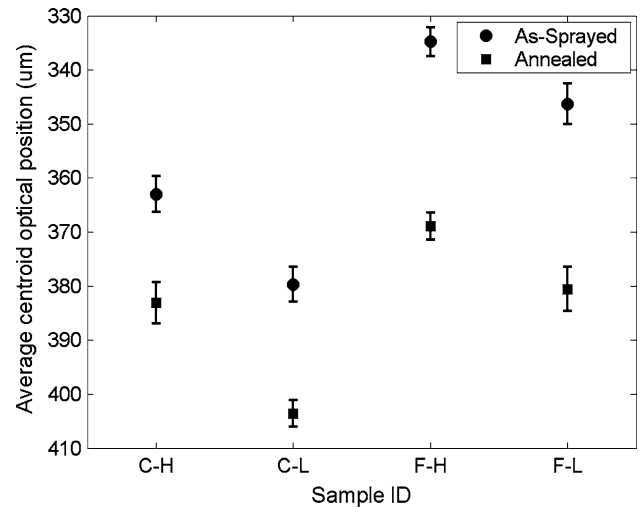

Fig. 6 Effect of absorption on light attenuation as measured by the average centroid position. The error bars shown are the statistical error made on the mean value calculated ($\sigma/n^{1/2}$). C-H—Coarse powder (Amperit 825.1) and High plasma torch power (35 kW), C-L—Coarse powder (Amperit 825.1) and Low plasma torch power (28 kW), F-H—Fine powder (Amperit 825.0) and High plasma torch power (35 kW) and F-L—Fine powder (Amperit 825.0) and Low plasma torch power (28 kW)

Before analyzing Fig. 6, it is important to notice that the average centroid optical positions of as-sprayed coatings are larger than the ones obtained in the previous calculation (Fig. 5). It can be explained by the depth range considered (or number N of points) in the calculation of the centroid position (Eq. 3). In previous calculation, N was limited to 1800 (image depth of 1800 μm) whereas $N = 2400$ (image depth of 2400 μm) for the present case in order to integrate the contribution of weakly attenuated light at larger depth for annealed coatings.

According to expectations, weaker light attenuation in annealed coatings is observed in Fig. 6. In fact, annealing has compensated the oxygen losses that occur in YSZ during the deposition process and reduced light absorption in the coatings, as measured by the centroid algorithm: the optical positions of centroid in annealed coatings are larger than the ones corresponding to as-sprayed coatings. Thus, a significant proportion of light attenuation inside coatings is due to light absorption in substoichiometric YSZ, even if the scattering regime dominates. Moreover, the absorption reduction after annealing does not modify the relative ranking of the coatings and, therefore, the conclusion regarding the relation between microstructure (density of interfaces) and light attenuation (centroid position) holds. However, the annealing effect seems more important on fine coatings (F-L and F-H) as compared to coarse coatings (C-L and C-H).

The latter observation can be understood according to the following explanations. The kinetics of oxygen losses at high temperature is faster for fine droplets (powder Amperit 825.0) since they have a larger specific area. As well, a finer microstructure (splats and pores) might also have a faster kinetics of oxygen reabsorption as compared to a coarse one. The fine coatings are probably less oxidized before annealing and probably more oxidized after, thus explaining the noted differences. The latter conclusion is based on the work of Inco (Ref 30) who showed that the change of valence states of zirconium, due to the reduction of ZrO_2 to ZrO_3, was responsible for darkening of TBC. Accordingly, we have observed that the fine coatings were the darkest/whitest before/after annealing, respectively.

3.3 YSZ Refractive Index

The evaluation of the index of refraction requires a few extra steps for sample preparation, which are described here. A YSZ coating was deposited under the spraying conditions depicted earlier, but with a slightly increased overspray cooling to maintain the surface temperature around 125 °C. The selected powder was Amperit 825.1 and the plasma torch power was 28 kW. The resulting coating has a thickness of 235 ± 11 μm and a porosity of $10.0 \pm 2.0\%$. The coating was detached from its steel substrate by acid dissolution and polished on both sides to form a wedge. Afterward, it was simply placed over a silicon wafer (Fig. 7) which provides two parallel reference surfaces for subsequent OCT cross-sectional imaging. Silicon was chosen for its high refractive index and its very
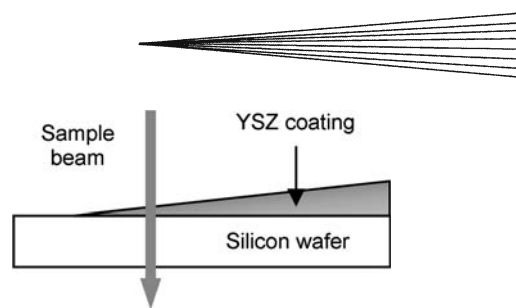
Fig. 7 Schematic representation of the YSZ coating wedge placed over a silicon wafer

low attenuation at the selected wavelength. Then, a single cross-sectional image of dimensions 10 mm wide and 3 mm deep, formed by 1000 interferogram envelopes (step size of 10 μm), is collected.

The resulting cross-sectional image is shown in Fig. 8(a). As in previous images, the coating/Si interface cannot be identified for a coating thickness larger than 50 μm, possibly due to multiple scattering events. However, the Si back surface has a decreasing amplitude with coating thickness that can be clearly observed. Since the Si wafer has very low attenuation, the back surface detection limit depends on the coating only. Also, this OCT image was used to identify two representative envelopes to evaluate the index of refraction of the coating. The first one was selected from a zone where the sample beam impinges only on the reference Si wafer, and the second one was extracted at a location where the sample beam gets through both the YSZ coating and the Si wafer (e.g., at the Si back surface detection limit). The corresponding envelopes are shown in Fig. 8(b) and (c). Dashed lines are plotted to appreciate the peak position shifts in optical depth at the coating top surface and at the Si wafer bottom surface. Therefore, the geometric coating thickness is given by the simple profilometry difference $z_1 - z_3$ and the back surface shift (involving the coating refractive index and thickness) is given by $z_4 - z_2$. Obviously, there should be an equivalent back shift for the Si wafer top surface peak position when light gets through the coating, but this peak is undetectable. Knowing that the coating contains about 10% porosity, the index of refraction n_{YSZ} of YSZ nontransformable tetragonal phase (which refers to a stable form of the tetragonal phase resulting from plasma spraying (Ref 31)) can be evaluated with the relation

$$[(0.9\,n_{YSZ} + 0.1\,n_{air}) - 1]e = d, \qquad (Eq\ 4)$$

where n_{air} is the air refractive index, $e = z_1 - z_3$ is the coating thickness and $d = z_4 - z_2$ is the Si wafer back surface shift. Thus, measuring in Fig. 8 a coating thickness $e = 96 \pm 5$ μm and a back surface shift $d = 55 \pm 5$ μm, the index of refraction of YSZ nontransformable tetragonal phase is evaluated as $n_{YSZ} = 1.64 \pm 0.1$. To the authors' knowledge, this is the first evaluation of the refractive index of YSZ nontransformable tetragonal phase. In comparison to the reported refractive index of about 2.1 for YSZ cubic phase (Ref 32), the value found seems quite small. However, the phase transition from cubic to tetragonal of pure evaporated zirconia (which comes with
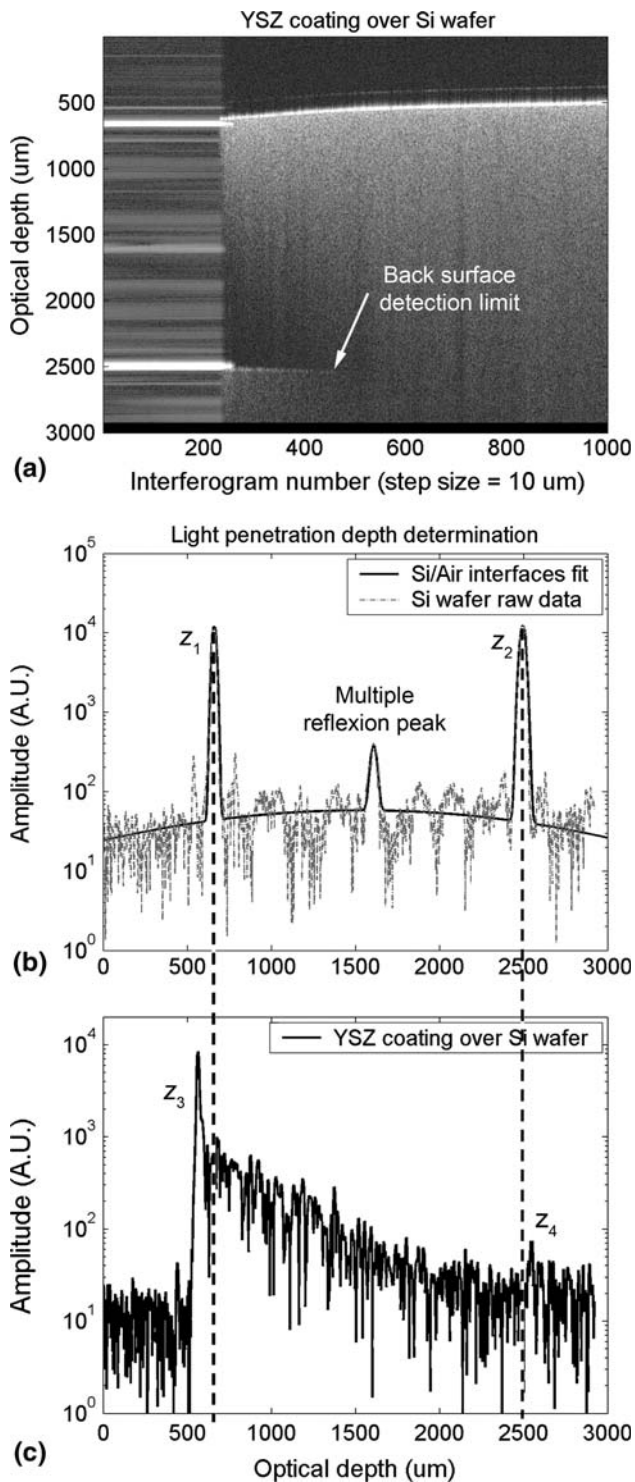
Fig. 8 (a) OCT cross-sectional image of an YSZ coating placed over a silicon wafer. (b) Silicon wafer reference interfaces (interferogram #5 in Fig. 8a). (c) Surface shifts observed when the beam crosses both the YSZ coating and the Si wafer (interferogram #445 in Fig. 8a)

a few percent increase in volume) has been found to influence significantly the refractive index, bringing it down to a value close to 1.7 (Ref 33). The same behavior

apparently affects the YSZ nontransformable tetragonal phase formed during plasma spraying.

4. Conclusions

In this study, OCT was evaluated as a NDE technique to characterize plasma-sprayed ceramic coating microstructure. It was found that light attenuation, as evaluated with the average centroid position, is a suitable OCT parameter to characterize the density of splat interfaces inside YSZ coatings. Indeed, light attenuation is stronger within fine coatings and coatings produced with a higher plasma torch power. Moreover, it was suggested that OCT light attenuation is strongly affected by the oxidation state of the material, which constitutes a limitation for an eventual in-line application of OCT. A limited probing depth (50 μm) compared to a typical YSZ coating thickness of 300-500 μm, as well as a limited axial resolution (11 μm in air, 6.7 μm in YSZ) compared to a typical splat thickness of 2-5 μm, represent two additional drawbacks of the technique. In fact, neither the coating/substrate interface nor the splat interfaces could be clearly distinguished and identified among multiple scattering. Further work should therefore be centered on shortening the light source coherence length (to improve the axial resolution and eventually clearly resolve splat interfaces), on increasing its power, and on reducing the speckle by implementing hardware or software solutions. Only then would the OCT 3-D imaging capability be useful to represent the coating microstructure and to resolve the interfaces of uppermost splats. Ideally, the latter measurement could provide interesting data related to splat thickness and interlamellar contact. Moreover, modeling light propagation inside the coatings should increase our understanding of the scattering phenomenon to clearly relate light attenuation not only to the density of interfaces, but also to the geometry of these interfaces or the scattering sites.
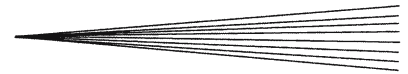
OCT was also used to measure the index of refraction of the YSZ nontransformable tetragonal phase formed during plasma spraying. The measured index of refraction was 1.64 ± 0.1.

Acknowledgments

References

1. X.Q. Cao, R. Vassen, and D. Stoever, Ceramic Materials for Thermal Barrier Coatings, *J. Eur. Ceram. Soc.*, 2004, **24**(1), p 1-10

2. J.R. Nicholls, Advances in Coating Design for High Performance Gas Turbines, *MRS Bull.*, 2003, **28**(9), p 659-670

3. N.B. Dahotre and S. Nayak, Nanocoatings for Engine Applications, *Surf. Coat. Technol.*, 2005, **194**(1), p 58-67

4. L. Sun, C.C. Berndt, K.A. Gross, and A. Kucuk, Material Fundamentals and Clinical Performance of Plasma-Sprayed Hydroxyapatite Coatings: A Review, *J. Biomed. Mater. Res., Part B*, 2001, **58**(5), p 570-592

5. S.P.S. Badwal and K. Foger, Solid Oxide Electrolyte Fuel Cell Review, *Ceram. Int.*, 1996, **22**(3), p 257-265

6. Z. Wang, A. Kulkarni, S. Deshpande, T. Nakamura, and H. Herman, Effects of Pores and Interfaces on Effective Properties of Plasma Sprayed Zirconia Coatings, *Acta Mater.*, 2003, **51**(18), p 5319-5334

7. A. Vincent and A. Moughil, Ultrasonic Characterization of Zirconia-based Thermal Barriers, *NDT Int.*, 1989, **22**(5), p 283-291

8. H.K. Wickramasinghe, Scanning Acoustic Microscopy: A Review, *J. Microsc.*, 1983, **129**(1), p 63-73

9. L. Pawloski, *The Science and Engineering of Thermal Spray Coatings*, Chichester, John Wiley & Sons, 1995, 414 p

10. C. Moreau, Towards a better control of thermal spray processes, *Thermal Spray: Meeting the Challenges of the 21st Century*, C. Coddet, Ed., May 25-29, 1998 (Nice, France), ASM International, 1998, p 1681-1693

11. D. Lian, Y. Suga, G. Shou, and S. Kurihara, An Ultrasonic Testing Method for Detecting Delamination of Sprayed Ceramic Coating, *J. Thermal Spray Technol.*, 1996, **5**(2), p 128-133

12. M. Viens, D. Drolet, A. Blouin, J.-P. Monchalin and C. Moreau, Nondestructive Characterization of Plasma-Sprayed Coatings by Laser Ultrasonics, *Thermal Spray: Practical Solutions for Engineering Problems*, C.C. Berndt, Ed., October 7-11, 1996 (Cincinnati, OH), ASM International, 1996, p 947-951

13. R. McPherson, A Model for the Thermal Conductivity of Plasma-Sprayed Ceramic Coatings, *Thin Solid Films*, 1984, **112**(1), p 89-95

14. S. Boire-Lavigne, C. Moreau, and R.G. St-Jacques, The Relationship Between the Microstructure and Thermal Diffusivity of Plasma-Sprayed Tungsten Coatings, *J. Thermal Spray Technol.*, 1995, **4**(3), p 261-267

15. J.I. Eldridge, C.M. Spuckler, J.A. Nesbitt, and K.W. Street, Health Monitoring of Thermal Barrier Coatings by Mid-Infrared Reflectance, *Ceram. Eng. Sci. Proc.*, 2003, **24**(3), p 511-516

16. F. Gitzhofer, C. Martin, and P. Fauchais, Contrôle par thermographie infrarouge de l'apparition de fissures dans un matériau céramique projeté par plasma et soumis à un cyclage thermique, *Rev. Gén. Therm.*, 1987, **301**, p 63-69

17. J. Ilavsky, G.G. Long, A.J. Allen, H. Herman, and C.C. Berndt, Use of Small-Angle Neutron Scattering for the Characterization of Anisotropic Structures Produced by Thermal Spraying, *Ceram.-Silik.*, 1998, **42**(3), p 81-89

18. A.J. Allen, J. Ilavsky, G.G. Long, J.S. Wallace, C.C. Berndt, and H. Herman, Microstructural Characterization of Yttria-Stabilized Zirconia Plasma-Sprayed Deposits Using Multiple Small-Angle Neutron Scattering, *Acta Mater.*, 2001, **49**(9), p 1661-1675

19. A. Kulkarni, Z. Wang, T. Nakamura, S. Sampath, A. Goland, H. Herman, A.J. Allen, J. Ilavsky, G.G. Long, J. Frahm, and R.W. Steinbrech, Comprehensive Microstructural Characterization and Predictive Property Modeling of Plasma-Sprayed Zirconia Coatings, *Acta Mater.*, 2003, **51**(9), p 2457-2475

20. S. Deshpande, A. Kulkarni, S. Sampath, and H. Herman, Application of Image Analysis for Characterization of Porosity in Thermal Spray Coatings and Correlation with Small Angle Neutron Scattering, *Surf. Coat. Technol.*, 2004, **187**(1), p 6-16

21. D. Huang, E.A. Swanson, C.P. Lin, J.S. Schuman, W.G. Stinson, W. Chang, M.R. Hee, T. Flotte, K. Gregory, C.A. Puliafito, and J.G. Fujimoto, Optical Coherence Tomography, *Science*, 1991, **254**(5035), p 1178-1181

22. J.P. Dunkers, F.R. Phelan, D.P. Sanders, M.J. Everett, W.H. Green, D.L. Hunston, and R.S. Parnas, The Application of Optical Coherence Tomography to Problems in Polymer Matrix Composites, *Optics Lasers Eng.*, 2001, **35**(3), p 135-147

23. M. Bashkansky, D. Lewis III, V. Pujari, J. Reintjes, and H.Y. Yu, Subsurface Detection and Characterization of Hertzian Cracks in Si_3N_4 Balls Using Optical Coherence Tomography, *NDT&E Int.*, 2001, **34**(8), p 547-555

24. R.J. Visher, W.A. Ellingson, M.D. Shields and A. Feuerstein, Laser-based Inspection of Thermal Barrier Coatings, *Proceedings of the 3rd International Surface Engineering Congress*, August 2-4, 2004 (Orlando, FL, USA), 2004, p 299-306

25. W.A. Ellingson, R.J. Visher, R.S. Lipanovich, and C.M. Deemer, Optical NDT Techniques for Ceramic Thermal Barrier Coatings, *Mater. Evaluation*, 2006, **64**(1), p 45-51

26. M.R. Hee, Optical Coherence Tomography: Theory, *Handbook of Optical Coherence Tomography*, B.E. Bouma and G.J. Tearney, Eds., (New York), Marcel Dekker, 2002, p 41-66

27. J.M. Schmitt, S.H. Xiang, and K.M. Yung, Speckle in Optical Coherence Tomography, *J. Biomed. Opt.*, 1999, **4**(1), p 95-105

28. M.J. Yadlowsky, J.M. Schmitt, and R.F. Booner, Multiple Scattering in Optical Coherence Microscopy, *Appl. Optics*, 1995, **34**(25), p 5699-5707

29. V. Debout, E. Bruneton, E. Meillot, S. Schelz, P. Abélard, P. Fauchais and A. Vardelle, Correlation Between Processing Parameters, Microstructure and Optical Properties for Plasma-Sprayed Yttria-Stabilized Zirconia Coatings, *Proceedings of the 17th International Symposium on Plasma Chemistry*, August 7-12, 2005 (Toronto, Canada), IPCS, 2005, Symposium CD

30. G.M. Inco, The Origin of Darkening in 8 wt% Yttria-Zirconia Plasma-Sprayed Thermal Barrier Coatings,, *J. Am. Ceram. Soc.*, 1991, **72**(2), p 381-386

31. P. Scardi, M. Leoni, and L. Bertamini, Influence of Phase Stability on the Residual Stress in Partially Stabilized Zirconia TBC Produced by Plasma Spray, *Surf. Coat. Technol.*, 1995, **76-77**, p 106-112

32. D.L. Wood, K. Nassau, and T.Y. Kometani, Refractive Index of Y_2O_3 Stabilized Cubic Zirconia: Variation with Composition and Wavelength, *Appl. Optics*, 1990, **29**(16), p 2485-2488

33. M.G. Krishna, K.N. Rao, and S. Mohan, Optical and Structural Characterization of Evaporated Zirconia Films, *Appl. Phys. Lett.*, 1990, **57**(6), p 557-559